ORIGINAL RESEARCH ARTICLE

Multifunctional Terahertz Absorber Based on Graphene-VO$_2$ Metamaterial with Linear Dichroism and Tunable Circular Dichroism

Zhe Chen[1] · Haowen Tang[1] · Zhonghua Chen[1] · Tao Shen[1,2] · Hui Zhang[3]

Abstract

This study proposes a multifunctional terahertz absorber utilizing graphene and vanadium dioxide as functional materials. By utilizing vanadium dioxide in the metallic state, the device achieves linear dichroism, with a maximum value of 0.8 at 1.75 THz, while in the insulating state, the introduction of graphene strips results in a chiral structure that achieves circular dichroism with tunable values ranging from 0 to 0.59 at 1.535 THz by regulating the graphene's Fermi level. The physical mechanism underlying the differential absorption is explained, and the influence of the device's structural parameters and incident angle on the performance is also investigated. This work provides a practical basis for the development of terahertz functional devices in polarization detection and near-field imaging.

Keywords Terahertz absorber · graphene · vanadium dioxide · linear dichroism · circular dichroism

Introduction

The unique frequency range of terahertz (THz) waves, which bridge the gap between microwave and infrared frequencies, has demonstrated immense potential in the fields of broadband communication, optical imaging, security detection and spectroscopy.[1–5] Metamaterials enhance the interaction between electromagnetic waves and matter by utilizing resonance and local field effects, greatly expanding the prospects of phase, amplitude and polarization control of electromagnetic waves, particularly THz waves.[6–8] Building upon this foundation, Landy et al. designed the first metamaterial-based absorber with a peak absorption rate over 88%,[9] thus solidifying metamaterials as an excellent choice for fabricating absorbers. In general, an ideal THz absorber can achieve adequate, controllable and selective absorption of THz waves. A polarization-dependent absorber is of great significance in polarization state detection and near-field imaging.[10–14] Linear dichroism (LD) can be understood as the differential absorption characteristics of a device for two linearly polarized waves that are perpendicular to each other. Similarly, circular dichroism (CD) refers to the differential absorption characteristics of a device for left-handed circularly polarized (LCP) and right-handed circularly polarized (RCP) waves.[15] The function of LD is mainly realized by introducing asymmetric patterns in the two orthogonal directions of the metamaterials, making asymmetrical micro-nanostructures when arranged,[16] while the function of CD can be realized by chiral metasurface units or the oblique incidence method.[17,18]

In order to expand the functionality and tunability of a single device, functional materials such as graphene,[19] Dirac semimetals,[20] photosensitive silicon[21] and vanadium dioxide (VO$_2$)[22] are introduced to metamaterial-based devices. Among them, as a Dirac semimetal, the conductivity of graphene can be adjusted by its carrier concentration, and its dielectric constant will be changed accordingly, thereby affecting its optical properties. Furthermore, VO$_2$ is a common phase-change material with a transition temperature of about 340 K. Once the temperature reaches about 340 K, its conductivity will increase nearly five orders, transforming

✉ Tao Shen
shentao@kust.edu.cn

✉ Hui Zhang
zhanghui@ynnu.edu.cn

1 Faculty of Information Engineering and Automation, Kunming University of Science and Technology, Kunming 650093, China

2 Yunnan Key Laboratory of Computer Technology Application, Kunming University of Science and Technology, Kunming 650500, China

3 Institute of Physics and Electronic Information, Yunnan Normal University, Kunming 650500, China

from an insulating phase to a metallic phase. This change of state can be achieved by thermal, electrical or optical stimulus.[23] By introducing these functional materials to the design of metamaterials, dynamical tunability of the absorber can be achieved. However, most of the reported tunable polarization-dependent absorbers only have the function of LD or CD. There are still few reports about tunable devices which can realize both LD and CD while maintaining good absorption performance.

In this work, we demonstrate a dynamically tunable bifunctional absorber that can switch between LD and CD, with a structure constructed by gold, VO₂, graphene and polyimide (PI). By modulating the conductivity of VO₂, the device can be switched between differential absorption of linearly polarized waves and circularly polarized waves. Furthermore, the CD characteristics generated by the device can be dynamically controlled by adjusting the Fermi level of graphene. The physical mechanisms underlying the generation of linear and circular dichroism were revealed through analysis of the surface current distributions and magnetic field distributions. Meanwhile, the impacts of variations in device structural parameters and incident angles on device performance were evaluated. Such a dichroic device with dynamic tunability and multifunctional characteristics offers a new idea and method for the design of polarization-dependent devices, and can also to some extent accelerate the development of fields such as polarization detection and near-field imaging.

Design and Method

The schematic diagram and geometric parameters of the designed device are shown in Fig. 1. The device unit is composed of gold, PI, graphene and VO₂, with a period P of 140 µm. On top of the gold substrate, there are three layers of PI as dielectric spacers with thicknesses of $H_1 = 10$ µm, $H_2 = 9$ µm and $H_3 = 16$ µm, respectively. The graphene layer with a thickness of 3.4 nm and a gold strip with a length L_1 of 120 µm and width W of 28 µm lying on top of it is sandwiched between the first and second layers of PI. The 0.2-µm-thick VO₂ layer is placed between the second and third layers of PI. The gold and graphene stripes at a 45° angle are located above the top PI layer. The length and width of the two strips are the same of $L_2 = 135$ µm and $W = 28$ µm. The thicknesses of all the gold layers are set to 0.2 µm.

The possible fabrication process of the proposed device is given below. Firstly, a gold layer with a thickness of 0.2 µm is evaporated on top of SiO₂/Si substrate. Then PI with the thickness of H_1 is spin-coated on top of the gold layer. After that, graphene film is transferred on the PI layer. Then a gold bar with width of W, length of L_1 and thickness of 0.2 µm is created by evaporation and lift-off. PI with a thickness of 0.2 µm is spin-coated on top of the graphene layer and the gold bar. VO₂ with a thickness of 0.2 µm is formed by sputtering. Then PI with a thickness
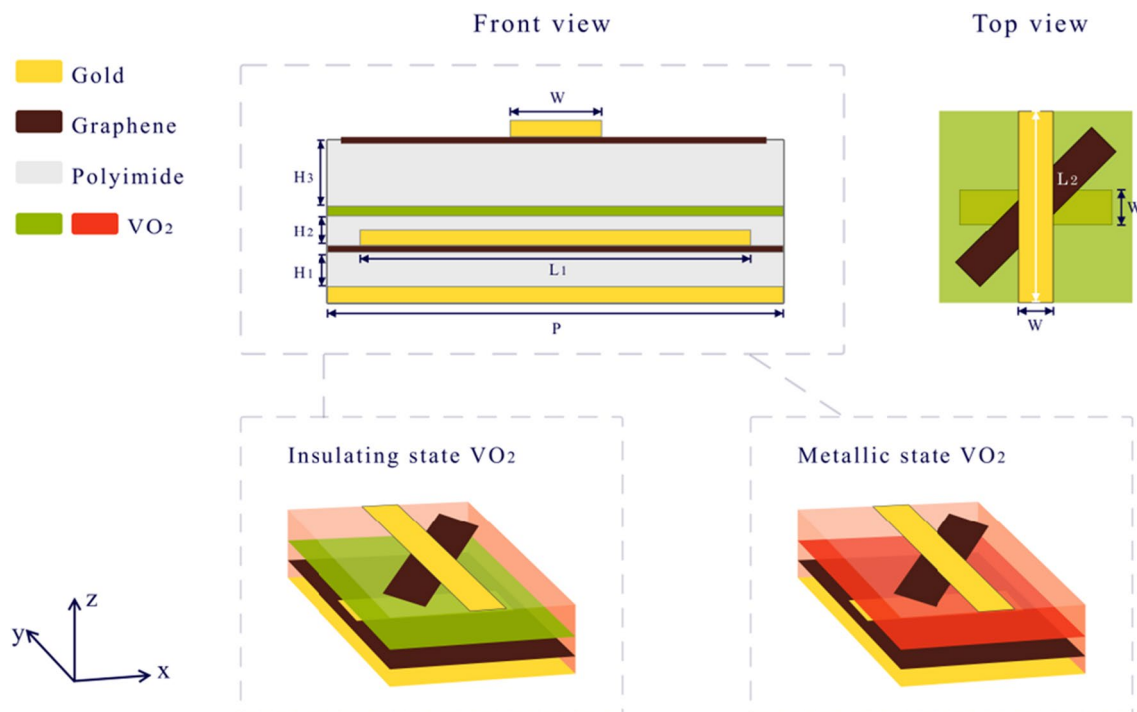

Fig. 1 Schematic diagram of the bifunctional device (Color figure online).

of H_3 is spin-coated on top of the VO$_2$ layer. Graphene film is transferred on the PI and patterned by reactive ion etching (RIE).[24] A gold bar with width of W, length of L_2 and thickness of 0.2 μm is created by evaporation and lift-off. Finally, the SiO$_2$/Si substrate can be removed by hydrofluoric acid (HF).

The performance of the proposed absorber is numerically investigated by a simulation tool based on the finite integration technique. In the simulation process, the perfect matching layer (PML) is used in the z direction, and the periodic boundary condition is set up in the x and y directions. The incident wave sources are x-polarized waves or y-polarized waves for the LD functional module and LCP waves or RCP waves for the CD functional module. During the simulation, the conductivity of gold is set as 4.561×10^7 S/m, the relative permittivity and loss tangent of PI are 3.5 and 0.0027, respectively. Meanwhile, in the THz regime, the relative permittivity of graphene can be calculated by $\varepsilon_G = 1 + \frac{i\sigma_G}{\omega \varepsilon_0 t_G}$, where σ_G represents the surface conductivity of graphene, ω is the angular frequency of the incident wave, ε_0 denotes the vacuum dielectric constant and t_G represents the thickness of the graphene layer. Generally, the conductivity of graphene is composed of both intra-band and inter-band transitions of the carriers, i.e., $\sigma_G = \sigma_{intra} + \sigma_{inter}$. However, in the terahertz band, the value of the inter-band carrier transition is much smaller than that of the intra-band transition, and can be a negligible quantity in this study. For this reason, the conductivity model of graphene can be simplified by the Kubo formula:[25,26]

$$\sigma_G \approx \sigma_{intra} = \frac{ie^2}{8\pi\hbar} \left\{ \frac{16k_B T}{\hbar(\omega + i\Gamma)} \ln\left[2\cosh\left(\frac{E_F}{2k_B T}\right)\right] \right\} \quad (1)$$

In Eq. 1, e is the electron charge, $\hbar$ denotes the reduced Planck constant and k_B is the Boltzmann constant, $T = 300$ K denotes the ambient temperature, Γ indicates the scattering rate of carriers with a value of 10^{12} s^{-1} and E_F represents the Fermi level of graphene. It is worth noting that the relaxation time of the graphene is set to 1 ps. The thickness of single-layer graphene in the simulation is set to 0.34 nm. By regulating the carrier concentration through an applied voltage, it is possible to adjust graphene's Fermi level.

During the numerical simulation process, it has been experimentally proven that the insulating state VO$_2$ can be considered as a dielectric with a permittivity of 9,[26] while the permittivity of metallic VO$_2$ can be characterized by the Drude model:[27]

$$\varepsilon(\omega) = \varepsilon_\infty - \frac{\omega_p^2 \cdot \frac{\sigma}{\sigma_0}}{\omega^2 + i\gamma\omega} \quad (2)$$

where $\varepsilon_\infty = 12$ denotes the relative permittivity of VO$_2$ at infinite frequency, and the reference plasma frequency of

VO$_2$ is $\omega_p = 1.4 \times 10^{15}$ rad/s. The conductivity of VO$_2$ is represented by σ, with reference conductivity σ_0 of 3×10^5 S/m and a collision frequency γ of 5.75×10^{13} rad/s. In this paper, only the fully insulating and fully metallic state of VO$_2$ is considered, in order to facilitate the exploration of the adjustable functions of the proposed device. Accordingly, the conductivity of the insulating state VO$_2$ film is set to 200 S/m and the conductivity of metallic state VO$_2$ is set to 4×10^5 S/m, which has been confirmed by experiments.[28]

The angle formed by the incident wave vector and the z-axis direction is referred to as the incident angle θ, with the default value being 0, indicating a vertically incident electromagnetic wave. The amplitude of the incident wave can be expressed as $E_x = 1 \times \sin\varphi$, $E_y = 1 \times \cos\varphi$, $E_z = 0$, where φ denotes the polarization angle of the incident wave.

As the proposed absorber works as a reflective device, the LD in this paper can be calculated by

$$LD = A_x - A_y = \left(1 - r^2_{xx} - r^2_{yx}\right) - \left(1 - r^2_{yy} - r^2_{xy}\right) \quad (3)$$

Here, A_x or A_y means the absorption rate of an x-polarized or y-polarized incident wave, r_{xx} or r_{yy} represents the co-polarization reflection coefficients of the x-polarized or y-polarized incident wave and r_{yx} or r_{xy} represents the cross-polarization reflection coefficients of x-polarized or y-polarized incident waves.

Meanwhile, the CD can be derived from

$$CD = A_- - A_+ = \left(1 - r^2_{--} - r^2_{+-}\right) - \left(1 - r^2_{++} - r^2_{-+}\right) \quad (4)$$

where A_- or A_+ means the absorption rate of RCP or LCP incident waves, r_{++} or r_{--} represents the co-polarization reflection coefficients of RCP or LCP incident wave and r_{+-} or r_{-+} represents the cross-polarization reflection coefficient of circularly polarized waves. To be noted, since the thickness of the Au substrate is much larger than the skin depth, the transmitted wave can be neglected.

Results and Discussion

Functional Module for Linear Dichroism

When the conductivity of VO$_2$ is 4×10^5 S/m, i.e., in the metallic state, and the Fermi level of the graphene is 0 eV, the device exhibits different absorption characteristics for x-polarized and y-polarized incident waves. The co-polarization reflection coefficients and cross-polarization reflection coefficients of the x-polarized and y-polarized incident waves are calculated and presented in Fig. 2a. At 1.75 THz, the co-polarization reflection coefficient of the x-polarized incident wave (r_{xx}) approaches zero, while the co-polarization reflection coefficient of the y-polarized incident wave
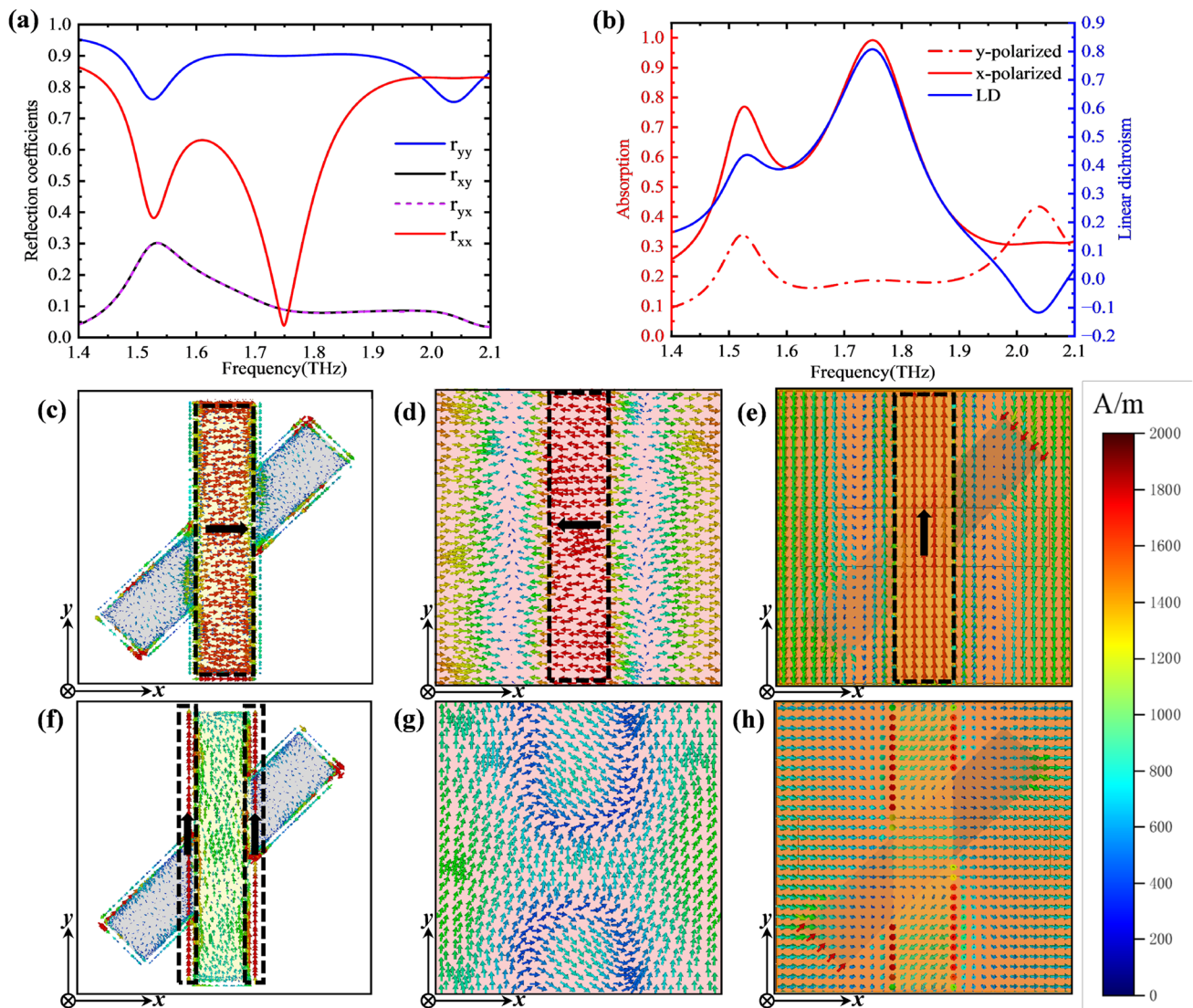
Fig. 2 (a) Reflection coefficients of the device under *x*-polarized and *y*-polarized incident waves when the conductivity of VO₂ is 4×10^5 S/m and E_F of graphene is 0 eV. (b) The absorption rate of *x*-polarized and *y*-polarized incident waves and the linear dichroism. The surface current distributions on (c) the top Au layer and (d) the VO₂ layer under *x*-polarized incident wave at 1.75 THz. (e) The magnetic field distribution under *x*-polarized incident wave at $z = 22$ μm, i.e., about 2 μm above the VO₂ layer. The surface current distribution on (f) the top Au layer and (g) the VO₂ layer under *y*-polarized incident wave at 1.75 THz. (h) The magnetic field distribution under *y*-polarized incident wave at $z = 22$ μm, i.e., about 2 μm above the VO₂ layer.

(r_{yy}) is approximately 0.9. Figure 2b displays the absorption rate and linear dichroism of the *x*-polarized and *y*-polarized incident waves, with a peak LD value of 0.8 at 1.75 THz.

To explain the mechanism behind the observed LD, we investigated the surface current distributions and magnetic field distributions of the device with *x*-polarized and *y*-polarized waves incident at 1.75 THz. As shown in Fig. 2c and d, anti-parallel surface currents are generated on the top Au layer and VO₂ layer when the incident wave is *x*-polarized, leading to magnetic resonance between the two layers as depicted in Fig. 2e. On the other hand, for a *y*-polarized incident wave at the same frequency, parallel currents

accumulate along the left and right sides of the upper Au strip, and no strong current is generated on VO₂ layer, resulting in no magnetic field resonance as shown in Fig. 2f, g and h. Therefore, for the *y*-polarized incident wave at 1.75 THz, a low absorption rate is formed due to the ohmic loss generated by the small amount of current.

In addition, the weaker LD peak that appears at 1.524 THz is also discussed by investigating the surface current distributions and magnetic field distributions to explain the physical mechanism. From Fig. 3a and b, it can be observed that when the device is under the excitation of *x*-polarized wave, three areas of strong induced current are generated
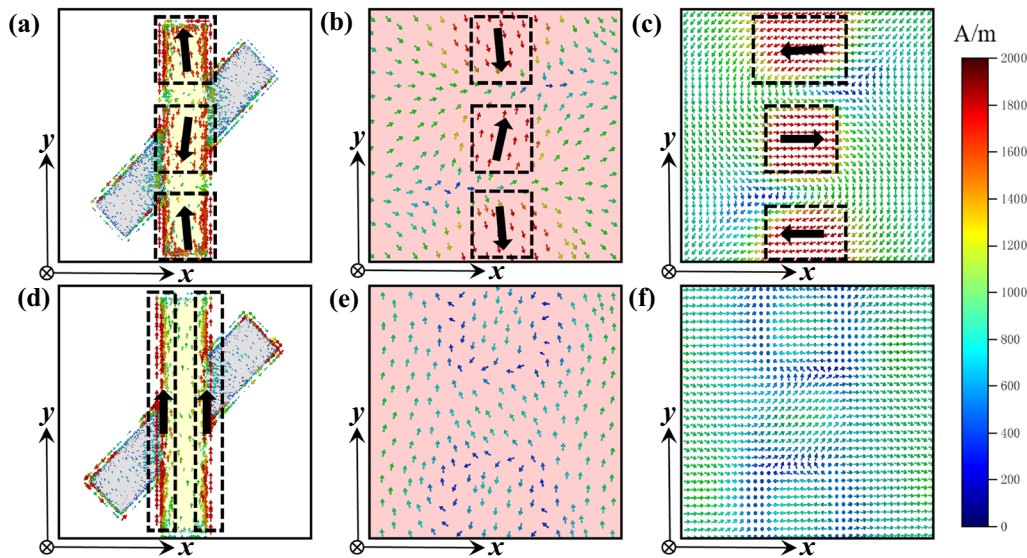
Fig. 3 The surface current distributions on (a) the top Au layer and (b) the VO$_2$ layer under x-polarized incident wave at 1.524 THz. (c) The magnetic field distribution under x-polarized incident wave at $z = 22$ μm. The surface current distribution on (d) the top Au layer and (e) the VO$_2$ layer under y-polarized incident wave at 1.524 THz. (f) The magnetic field distribution under y-polarized incident wave at $z = 22$ μm.
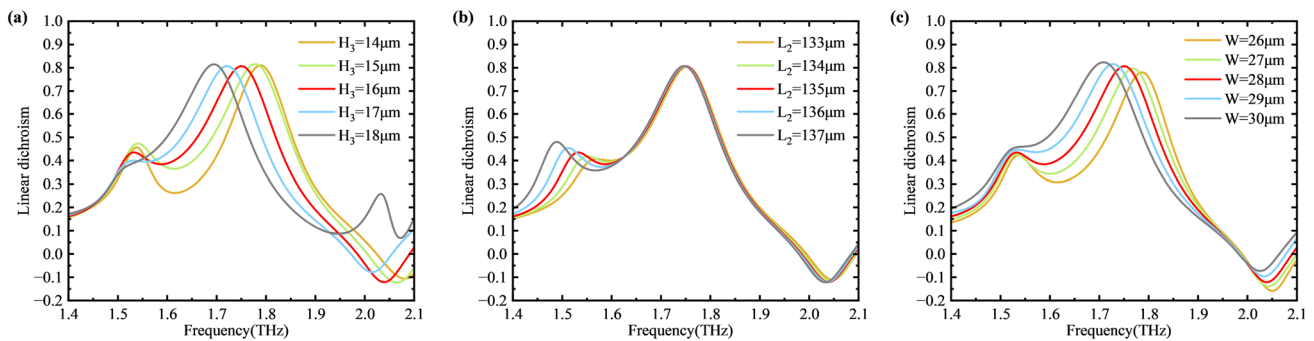

Fig. 4 The effects of structural parameters on linear dichroism performance. (a) The thickness of the upper PI layer. (b) The length of the top gold strip and graphene strip. (c) The width of the top gold strip and graphene strip.

both on the top gold bar and the VO$_2$ film, it is worth noting that the current in the corresponding region is anti-parallel. Therefore, it can be concluded that magnetic resonance is generated between the two layers, as shown in Fig. 3c, which thus leads to the relatively high absorption. When the excitation source is a y-polarized wave, it can be observed from Fig. 3d and e that surface currents are accumulated along the left and right sides of the upper gold bar, while there is no significant current in the VO$_2$ film. Therefore, it can be concluded that the main reason for generating a relatively small absorption peak is due to electrical resonance. Finally, a LD peak appears due to the differential absorption at 1.524 THz.

Next, the impacts of structural parameters on the LD performance are examined. With VO$_2$ in the metallic state, the electromagnetic response inside the device mainly occurs

above the VO$_2$ layer due to the skin depth effect. Thus, the influences of three structural parameters H_3, L_2 and W on the device performance are studied. The increased thickness of the upper polyimide layer results in a red shift in the LD curve and the peak values barely change, as depicted in Fig. 4a. The results presented in Fig. 4b indicate that maintaining L_2 within the range of 133–137 μm preserves both the LD peak values and the corresponding frequencies. Furthermore, as demonstrated in Fig. 4c, a slight decrease in LD peak values from 0.83 to 0.77 is observed with an increase in W from 26 μm to 30 μm, accompanied by a frequency shift from 1.70 THz to 1.79 THz.

The LD values of the device for obliquely incident terahertz wave are also investigated, with the result shown in Fig. 5. To obtain Fig. 5, the absorption rates of x-polarized
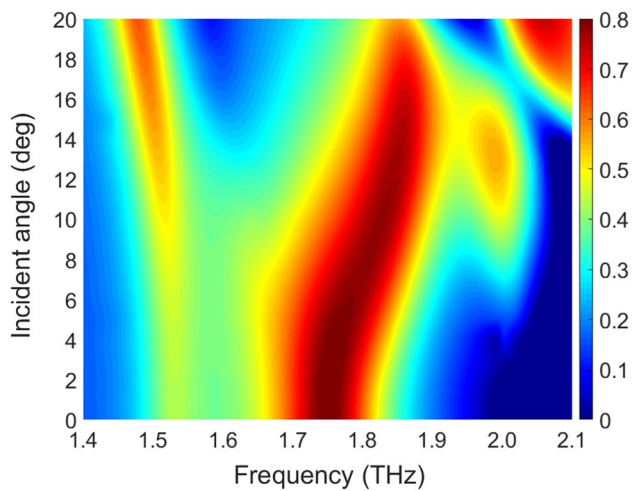
Fig. 5 Effects of incident angle on the performance of LD.

and y-polarized waves at different incident angles are obtained first, and then the difference between them is solved to determine the effects of incident angle on the LD performance. For incident angles less than 18°, the peak value of LD remains greater than 0.7 and the corresponding frequency shows blue shift with increased incident angle.

Functional Module for Circular Dichroism

When the conductivity of VO$_2$ is 200 S/m, i.e., in the insulating state, and the Fermi level of the graphene is 1 eV, the gold strip and the graphene strip with an included 45° angle on the top form a chiral structure. As a result, there is a significant difference in the absorption rates of LCP and RCP incidences. Figure 6a shows the co-polarization reflection coefficients and cross-polarization reflection coefficients of LCP and RCP incident waves. At 1.535 THz, the minimum value less than 0.1 of the co-polarization reflection coefficient for RCP incident wave r_{--} is achieved, while the LCP component r_{++} is about 0.77. Figure 6b displays the absorption rate and circular dichroism of the two circularly polarized waves, where the RCP incident wave has an absorption rate of 0.99, whereas the LCP absorption rate is only about 0.4 at 1.535 THz. It can be found that the chiral structure exhibits a CD value of up to 0.59 at 1.535 THz. This indicates that the chiral structure has a stronger reflecting response to the LCP waves and a stronger absorbing response to RCP waves.

In order to gain a better understanding of CD, the surface current distributions and magnetic field distributions of the device at 1.535 THz are analyzed. The surface current distributions of the upper and lower graphene and Au layers are shown in Fig. 6c and d, respectively. As indicated by the black rectangle boxes, five regions of anti-parallel currents can be observed, thus magnetic resonances are formed

between these two layers as shown in Fig. 6e, leading to a strong absorption of RCP incident waves at 1.535 THz. On the contrary, when LCP waves are incident on the device, currents are accumulated at the two ends of the top graphene strip and the middle of the lower gold strip as shown in Fig. 6f and g, which cannot meet the condition for the formation of magnetic resonance, as shown in Fig. 6h. As a result, a relatively small absorption is formed due to the ohmic loss caused by the currents.

The tunability of CD characteristic modulated by the E_F of graphene is also investigated, with the results shown in Fig. 7. It can be seen that increasing the E_F of graphene leads to a rise in its CD peak value, together with a significant blue shift. When $E_F = 0.2$ eV, the CD at 1.535 THz approaches zero. As the Fermi level increases to 1 eV, the CD value at 1.535 THz reaches its maximum of 0.59. The modulation range of the CD value at this frequency is between 0 and 0.59.

Furthermore, the impact of structural parameters on the CD performance of the device is analyzed. The CD values are computed for various values of W, ranging from 26 μm to 30 μm, as illustrated in Fig. 8a. The peak value of CD exhibits a non-monotonic behavior with the increase of W, showing a slight red shift. A maximum CD value of 0.59 is achieved at 1.535 THz when W equals to 28 μm. L_2 has a negligible effect on the peak CD value and the corresponding frequencies, as illustrated in Fig. 8b. From the aforementioned analysis, the magnetic resonance mainly occurs at the upper two layers of PI, accompanied by dielectric loss. The impacts of PI layer thicknesses H_2 and H_3 on CD performance are analyzed, as shown in Fig. 8c and d. The CD first increases to a maximum of 0.59 at $H_2 = 9$ μm and then decreases as H_2 increases. Similarly, the change of CD with H_3 follows the same trend as H_2 and the maximum CD is obtained at $H_3 = 16$ μm.

Finally, Fig. 9 illustrates the impact of incidence angle on CD performance. The peak CD value remains greater than 0.5 with incident angles from 0° to 5°. As the incidence angle increases, the CD will gradually decrease and split into two relatively weak peaks.

Comparing the performance of the proposed device's absorption peak, tunability, maximum LD and CD with those of other published polarization-dependent absorbers further highlights the innovation of this study, as shown in Table I. All of these works are based on numerical simulation. On this premise, the metasurface in the work by Cui et al.[12] exhibits a high LD value, but it can only work in LD mode with a fixed working frequency. The metasurface reported by Li et al.[15] can perform CD with tunability and a maximum CD value of 0.77, but it also has just one function. Wang et al.[29] propose a multiband CD device, but it has no active material to make it a dynamically tunable device. Similar to that proposed by Li et al.,[15] the device proposed
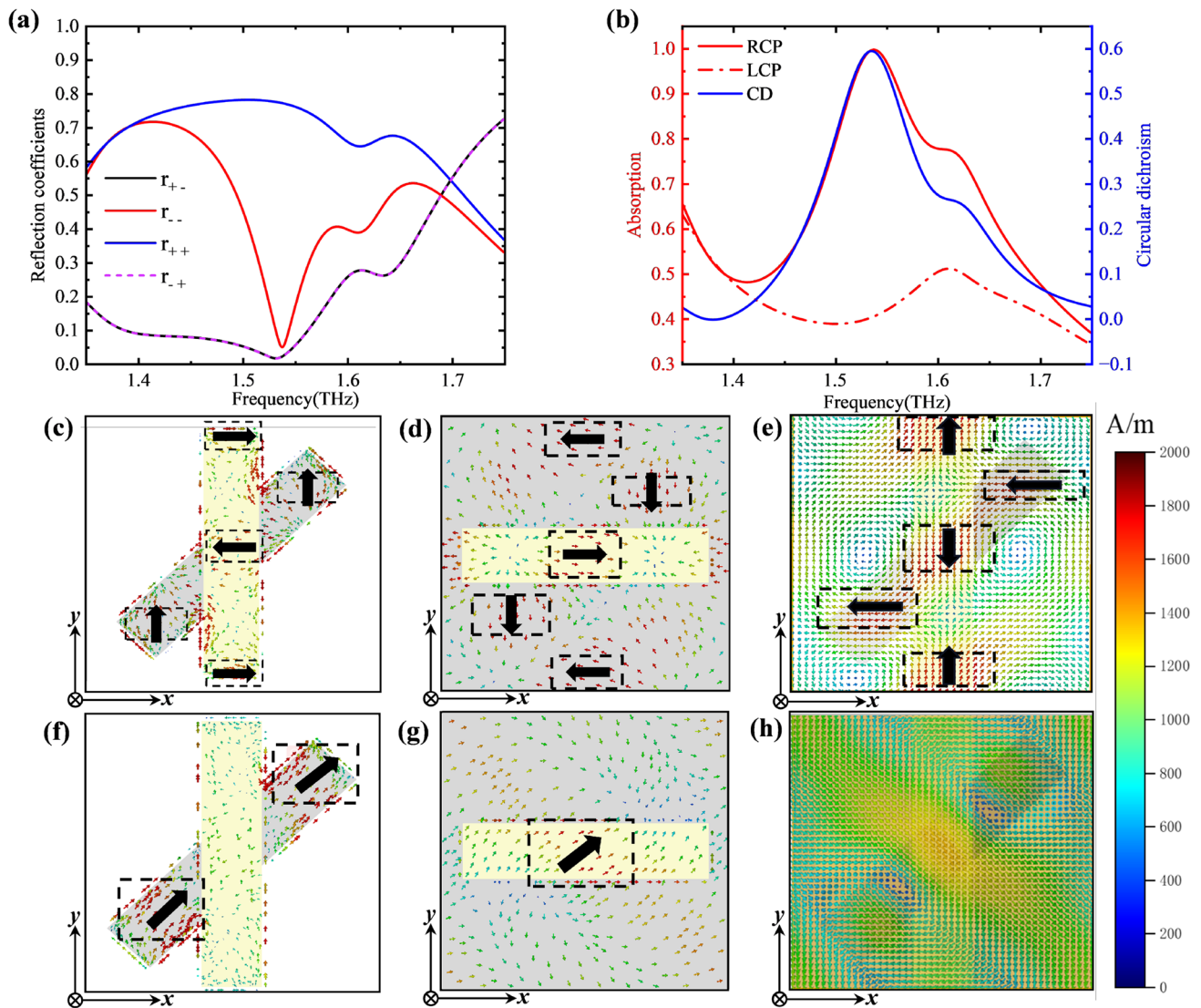
Fig. 6 (a) Reflection coefficients for co-polarization and cross-polarization of the device under RCP and LCP incident waves, respectively, with E_F of graphene setting to 1 eV. (b) Absorption rate and circular dichroism of RCP and LCP incident waves. Surface current distributions on the (c) upper graphene and Au layer and (d) lower graphene and Au layer under RCP wave incidence at 1.535 THz. (e) The magnetic field distribution under the RCP incident wave at $z = 22$ μm. The surface current distributions on the (f) top graphene and Au layer and (g) the lower graphene and gold layer under LCP wave incidence at 1.535 THz. (h) Magnetic field distribution under LCP incident wave at $z = 22$ μm.

by Li et al.[30] exhibits a tunable CD controlled by the Fermi level of the graphene, but the device has only one function. The metasurface proposed by Asgari and Fabritius[31] has a relatively high tunable LD performance, but cannot work as a CD device. Similarly, a device with CD up to 0.58 is described by Qin et al.,[32] but it has no tunability or multi-functionality. Although the dichroic metasurface reported by

Li et al.[33] achieves the dual function of both tunable CD and LD, the LD and CD amplitudes implemented by the device are not high enough, reaching only 0.76 and 0.45, respectively. All in all, the proposed device in this paper can realize both LD and CD, and the CD peak value is tunable from 0 to 0.59, which to a certain extent fills the gap in the current research of polarization-dependent THz devices.
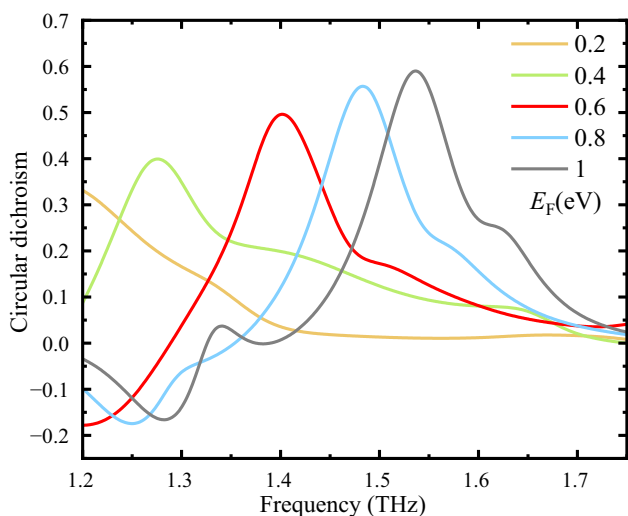
Fig. 7 Simulation results of CD for varying Fermi levels of graphene in the range of 0.2–1 eV (Color figure online).
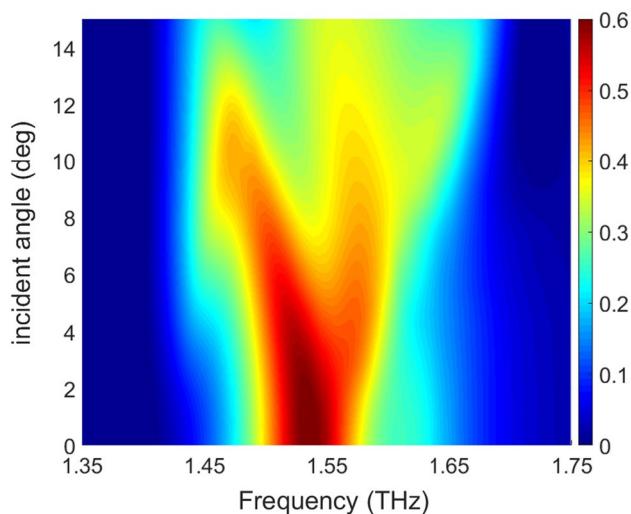

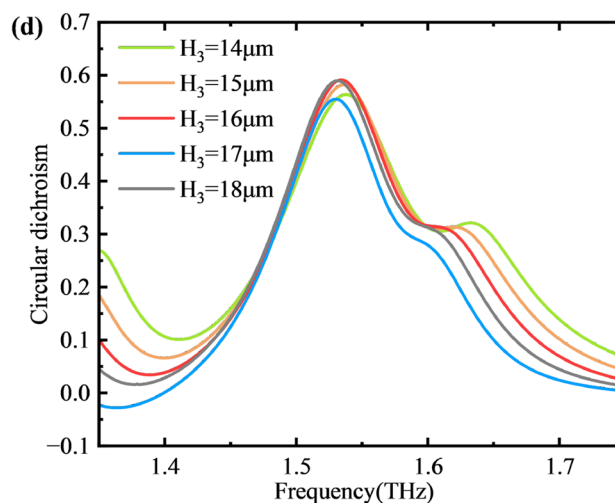**Fig. 9** Effects of incident angle on the performance of CD.
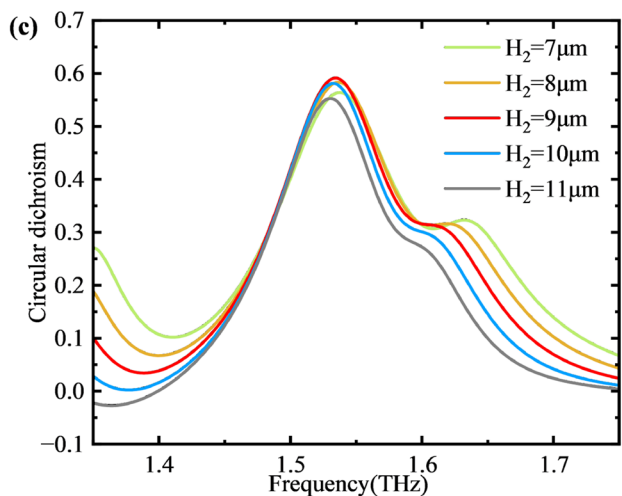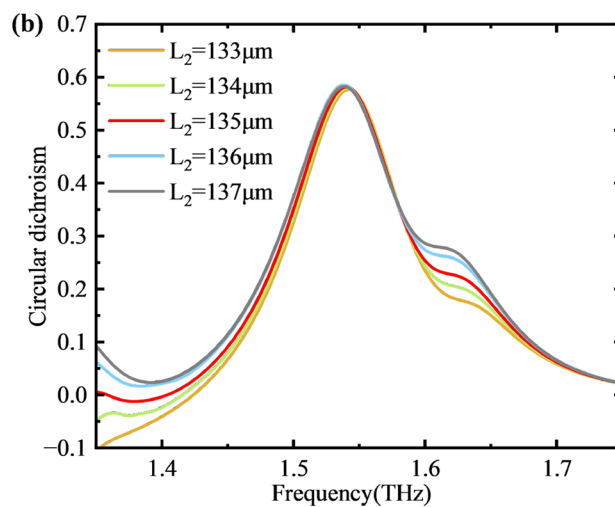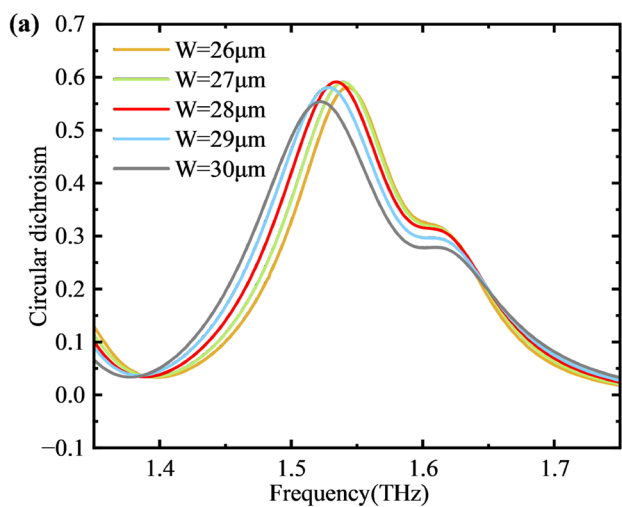

Fig. 8 The effects of structural parameters on CD performance of the device. (a) The width of the top gold strip and graphene strip. (b) The length of the top gold strip and graphene strip. (c) The thickness of the middle PI layer. (d) The thickness of the upper PI layer (Color figure online).

Table I Comparison of devices' functional materials, absorption, tunability and LD/CD performance

References	Functional materials	Absorption peak	Tunability	Maximum LD/CD
12	No	> 0.95	No	0.9 (LD)
15	Graphene	> 0.97	Yes	0.77 (CD)
29	No	> 0.99	No	0.58 and 0.86 (CD)
30	Graphene	> 0.92	Yes	0.59 (CD)
31	Graphene	> 0.99	Yes	0.9 (LD)
32	No	> 0.99	No	0.58 (CD)
33	Graphene + VO_2	> 0.99	Yes	0.76 (LD) 0.45 (CD)
This work	Graphene + VO_2	> 0.99	Yes	0.8 (LD) 0.59 (CD)

Conclusion

In conclusion, we have presented a metamaterial-based bifunctional THz polarization-dependent absorber that exhibits both LD and CD properties. The absorber mode can be switched using phase change material VO_2, while the device performance can be dynamically modulated using graphene. The absorption rate and dichroism performance are calculated and the mechanisms of differential absorption are analyzed under the two operating modes of the proposed absorber. The maximum absorption rates are close to 100% in both modes, the maximum LD value is 0.8 at 1.75 THz and the maximum CD value is 0.59 at 1.535 THz. By manipulating the Fermi level of graphene, it is possible to adjust the circular dichroism between the values of 0 and 0.59. The linear dichroism and circular dichroism performance of the device are also estimated under oblique incidence. The results demonstrate that this device is sensitive to incident angle and can retain its performance in a constrained range of incident angle. These results provide new insights for the design of multifunctional polarization-dependent absorbers and the advancement of dichroic devices.

Conflict of interest The authors declare that they have no conflict of interest.

References

1. T.J. Cui, S. Liu, and L.L. Li, Information entropy of coding metasurface. *Light Sci. Appl.* 5, e16172 (2016).
2. Z.Q. He and X.J. Yuan, Cascaded channel estimation for large intelligent metasurface assisted massive MIMO. *IEEE Wirel. Commun. Lett.* 9, 210–214 (2020).
3. X. Jiang, H. Chen, Z.Y. Li, H.K. Yuan, L.Y. Cao, Z.F. Luo, K. Zhang, Z.H. Zhang, Z.Q. Wen, L.G. Zhu, X. Zhou, G.F. Liang, D.S. Ruan, L.H. Du, L.F. Wang, and G. Chen, All-dielectric metalens for terahertz wave imaging. *Opt. Express* 26, 14132–14142 (2018).
4. X.J. Ni, A.V. Kildishev, and V.M. Shalaev, Metasurface holograms for visible light. *Nat. Commun.* 4, 6 (2013).
5. S. Taravati and G.V. Eleftheriades, Pure and linear frequency-conversion temporal metasurface. *Phys. Rev. Appl.* 15, 12 (2021).
6. T. Chung, H. Wang, and H. Cai, Dielectric metasurfaces for next-generation optical biosensing: a comparison with plasmonic sensing. *Nanotechnology* 34, 402001 (2023).
7. Y. Cui and Y. Jiang, Dual-band tunable and strong circular dichroism in a metal-graphene hybrid zigzag metasurface. *Opt. Express* 30, 42614–42623 (2022).
8. Y. Cui, X. Wang, B. Ren, H. Jiang, and Y. Jiang, High-efficiency and tunable circular polarization selectivity in photosensitive silicon-based zigzag array metasurface. *Opt. Laser Technol.* 156, 108453 (2022).
9. N.I. Landy, S. Sajuyigbe, J.J. Mock, D.R. Smith, and W.J. Padilla, Perfect metamaterial absorber. *Phys. Rev. Lett.* 100, 207402 (2008).
10. Y. Cai, Y. Guo, Y. Zhou, X. Huang, G. Yang, and J. Zhu, Tunable dual-band terahertz absorber with all-dielectric configuration based on graphene. *Opt. Express* 28, 31524–31534 (2020).
11. Z. Chen, J. Chen, H. Tang, T. Shen, and H. Zhang, Dynamically switchable broadband and triple-band terahertz absorber based on a metamaterial structure with graphene. *Opt. Express* 30, 6778–6785 (2022).
12. Z. Cui, D. Zhu, L. Yue, H. Hu, S. Chen, X. Wang, and Y. Wang, Development of frequency-tunable multiple-band terahertz absorber based on control of polarization angles. *Opt. Express* 27, 22190–22197 (2019).
13. X. Huang, F. Yang, B. Gao, Q. Yang, J. Wu, and W. He, Metamaterial absorber with independently tunable amplitude and frequency in the terahertz regime. *Opt. Express* 27, 25902–25911 (2019).
14. K.-D. Xu, J. Li, A. Zhang, and Q. Chen, Tunable multi-band terahertz absorber using a single-layer square graphene ring structure with T-shaped graphene strips. *Opt. Express* 28, 11482–11492 (2020).
15. F.Y. Li, T.T. Tang, Y.H. Mao, L. Luo, J. Li, J.X. Xiao, K.L. Liu, J. Shen, C.Y. Li, and J.Q. Yao, Metal-graphene hybrid chiral metamaterials for tunable circular dichroism. *Ann. Phys.* 532, 2000065 (2020).
16. B.X. Wang, G.Z. Wang, X. Zhai, and L.L. Wang, Polarization tunable terahertz metamaterial absorber. *IEEE Photonics J.* 7, 1–7 (2015).

17. Z. Wang, F. Cheng, T. Winsor, and Y. Liu, Optical chiral metamaterials: a review of the fundamentals, fabrication methods and applications. *Nanotechnology* 27, 412001 (2016).

18. J. Xu, J. Tang, M. Chen, C. Teng, S. Deng, Y. Cheng, S. Qu, and L. Yuan, Actively tunable linear and circular dichroic metamirrors based on single-layer graphene. *Opt. Express* 31, 381–395 (2023).

19. L. Chen and Z. Song, Simultaneous realizations of absorber and transparent conducting metal in a single metamaterial. *Opt. Express* 28, 6565–6571 (2020).

20. X.L. Wu, Y. Zheng, Y. Luo, J.G. Zhang, Z. Yi, X.W. Wu, S.B. Cheng, W.X. Yang, Y. Yu, and P.H. Wu, A four-band and polarization-independent BDS-based tunable absorber with high refractive index sensitivity. *Phys. Chem. Chem. Phys.* 23, 26864–26873 (2021).

21. Y.Q. Tong, S.Y. Wang, X.X. Song, L. Yang, J.Q. Yao, Y.X. Ye, Y.P. Ren, Y.T. Zhang, S.S. Xin, and X.D. Ren, Multi-band tunable terahertz absorber based on metamaterial. *Int. J. Infrared Millim. Waves* 39, 735–741 (2020).

22. T. Driscoll, S. Palit, M.M. Qazilbash, M. Brehm, F. Keilmann, B.G. Chae, S.J. Yun, H.T. Kim, S.Y. Cho, N.M. Jokerst, D.R. Smith, and D.N. Basov, Dynamic tuning of an infrared hybrid-metamaterial resonance using vanadium dioxide. *Appl. Phys. Lett.* 93, 024101 (2008).

23. L. Kang, H.G. Bao, S.D. Campbell, P.L. Werner, D.H. Werner, S.X. Wang, C.F. Cai, M.H. You, F.Y. Liu, M.H. Wu, S.Z. Li, Tunable broadband terahertz metamaterial absorbers based on VO₂, in *2020 IEEE International Symposium on Antennas and Propagation and North American Radio Science Meeting* (2020), pp. 729–730.

24. G. Xie, Z. Shi, R. Yang, D. Liu, W. Yang, M. Cheng, D. Wang, D. Shi, and G. Zhang, Graphene edge lithography. *Nano Lett.* 12(9), 4642–4646 (2012).

25. M. Jablan, H. Buljan, and M. Soljačić, Plasmonics in graphene at infrared frequencies. *Phys. Rev. B* 80, 245435 (2009).

26. T.T. Lv, Y.X. Li, H.F. Ma, Z. Zhu, Z.P. Li, C.Y. Guan, J.H. Shi, H. Zhang, and T.J. Cui, Hybrid metamaterial switching for manipulating chirality based on VO₂ phase transition. *Sci. Rep.* 6, 23186 (2016).

27. Y. Zhu, Y. Zhao, M. Holtz, Z. Fan, and A.A. Bernussi, Effect of substrate orientation on terahertz optical transmission through VO₂ thin films and application to functional antireflection coatings. *J. Opt. Soc. Am. B* 29, 2373–2378 (2012).

28. G. Zhou, P. Dai, J. Wu, B. Jin, Q. Wen, G. Zhu, Z. Shen, C. Zhang, L. Kang, W. Xu, J. Chen, and P. Wu, Broadband and high modulation-depth THz modulator using low bias controlled VO₂-integrated metasurface. *Opt. Express* 25, 17322–17328 (2017).

29. H. Wang, H.Q. Zhou, T.H. Li, Z. Qin, C.C. Li, X. Li, Y.F. Li, J.Q. Zhang, S.B. Qu, and L.L. Huang, Tailoring circular dichroism via the Born-Kuhn model for meta-holograms. *Sci. China Phys. Mech. Astron.* 65, 104212 (2022).

30. J. Li, J. Li, Y. Yang, J. Li, Y. Zhang, L. Wu, Z. Zhang, M. Yang, C. Zheng, J. Li, J. Huang, F. Li, T. Tang, H. Dai, and J. Yao, Metal-graphene hybrid active chiral metasurfaces for dynamic terahertz wavefront modulation and near field imaging. *Carbon* 163, 34–42 (2020).

31. S. Asgari and T. Fabritius, Graphene-based multiband chiral metamaterial absorbers comprised of square split-ring resonator arrays with different numbers of gaps, and their equivalent circuit model. *IEEE Access* 10, 63658–63671 (2022).

32. W.-G. Qin, W.-P. Zhang, L. Li, Y.-J. Huang, and Z.-W. Xie, Numerical simulation research of circular dichroism based on a catenary-shaped ultrathin metasurface. *J. Opt. Soc. Am. B* 39, 1543–1548 (2022).

33. J. Li, C. Zheng, J. Li, H. Zhao, X. Hao, H. Xu, Z. Yue, Y. Zhang, and J. Yao, Polarization-dependent and tunable absorption of terahertz waves based on anisotropic metasurfaces. *Opt. Express* 29, 3284–3295 (2021).